OPEN

Correspondence and
requests for materials
should be addressed to
J.H.K. (jhk@uow.edu.
au) or J.-W.L.
(jjong277@kier.re.kr)

* These authors
contributed equally to
this work.

One-dimensional manganese-cobalt oxide nanofibres as bi-functional cathode catalysts for rechargeable metal-air batteries

Kyu-Nam Jung[1]*, Soo Min Hwang[2]*, Min-Sik Park[3], Ki Jae Kim[3], Jae-Geun Kim[3], Shi Xue Dou[2], Jung Ho Kim[2] & Jong-Won Lee[1]

[1]New and Renewable Energy Research Division, Korea Institute of Energy Research, 152 Gajeong-ro, Yuseong-gu, Daejeon 305-343, Republic of Korea, [2]Institute for Superconducting and Electronic Materials, Australian Institute for Innovative Materials, University of Wollongong, Innovation Campus, North Wollongong, New South Wales 2500, Australia, [3]Advanced Batteries Research Center, Korea Electronics Technology Institute, 68 Yatap-dong, Bundang-gu, Seongnam 463-816, Republic of Korea.

Rechargeable metal-air batteries are considered a promising energy storage solution owing to their high theoretical energy density. The major obstacles to realising this technology include the slow kinetics of oxygen reduction and evolution on the cathode (air electrode) upon battery discharging and charging, respectively. Here, we report non-precious metal oxide catalysts based on spinel-type manganese-cobalt oxide nanofibres fabricated by an electrospinning technique. The spinel oxide nanofibres exhibit high catalytic activity towards both oxygen reduction and evolution in an alkaline electrolyte. When incorporated as cathode catalysts in Zn-air batteries, the fibrous spinel oxides considerably reduce the discharge-charge voltage gaps (improve the round-trip efficiency) in comparison to the catalyst-free cathode. Moreover, the nanofibre catalysts remain stable over the course of repeated discharge-charge cycling; however, carbon corrosion in the catalyst/carbon composite cathode degrades the cycling performance of the batteries.

I n recent years, there has been a strong demand for advanced rechargeable battery systems with high energy storage capability. Among the various energy storage technologies under development, the metal-air battery, in which a metal anode (Li, Zn, Al, *etc.*) is coupled with an air-breathing porous cathode, delivers much higher specific energy compared to conventional battery chemistries such as lithium-ion batteries[1–5]. The metal-air battery operates *via* electrochemical reactions involving oxygen supplied from the ambient air on the cathode, *i.e.*, the oxygen reduction reaction (ORR) during discharge and the oxygen evolution reaction (OER) during charge[2–5]. Unfortunately, most metal-air batteries suffer from sluggish ORR-OER kinetics and thus display very large voltage gaps (low round-trip efficiency) for discharge-charge cycling as well as poor power capability[2–5]. There has been extensive research on catalytic materials that are capable of promoting both the ORR and the OER. Precious metals, such as Pt, Au, Pd, and Ag, possess superb catalytic properties[5–8]; however, high material costs and scarcity prohibit their widespread use in large-scale applications. Recently, a greater focus has been directed towards non-precious metal oxides[9–18] and carbonaceous materials incorporated with heteroatoms (metals, N, O, P, S, *etc.*)[19–24]. In particular, mixed transition metal oxides have been regarded as cost-effective catalysts for metal-air batteries with alkaline electrolytes, since they are known to have reasonable catalytic activity and structural stability as well as acceptable electronic properties[10,12,14–16,18].

Morphology-controllable synthesis has aroused great interest in the field of catalysis owing to the possibility of improving electrochemical properties by tailoring morphologies and surface structures on the nanoscale. In particular, one-dimensional (1D) fibrous nanomaterials exhibit unique properties that make them suitable for use as catalysts, for instance, high surface area-to-volume ratios, short lengths for charge transport/diffusion in the radial direction, and low resistance to the flow of gas and liquid through fibre bundles and/or porous fibres. Specific examples demonstrating the feasibility of fibrous materials in metal-air batteries include Co_3O_4 nanofibres employed as OER catalysts in a non-aqueous Li-O_2 battery[15] and $NiCo_2O_4$ nanofibres for bi-functional ORR-OER catalysts in an aqueous Zn-air battery[18]. 1D fibrous materials can be fabricated by a wide variety of

synthesis techniques, *e.g.*, electrospinning[25,26], solvothermal[27], template-directed[28], and self-assembly techniques[29]. Among these, electrospinning is a remarkably simple and versatile process for generating fibrous materials with controlled morphologies[25,26].

In an effort to develop cost-effective electrocatalysts with high bi-functionality for use in rechargeable metal-air batteries, herein, we report 1D metal oxide nanofibres based on spinel-type manganese-cobalt oxides ($MnCo_2O_4$ and $CoMn_2O_4$). The fibrous spinel oxide catalysts were fabricated *via* an electrospinning technique combined with an optimized post-heat-treatment, and their catalytic properties towards the ORR and OER were investigated in an aqueous alkaline electrolyte. As will be shown later, the fibrous spinel oxides exhibit excellent catalytic properties for both the ORR and the OER, and reduce the discharge-charge voltage gaps of Zn-air batteries, leading to enhanced round-trip efficiency. Also, the fibrous catalysts proved to be stable under accelerated potential cycling conditions.

Results

Synthesis and characterisation of 1D $MnCo_2O_4$ and $CoMn_2O_4$ nanofibres. The $MnCo_2O_4$ and $CoMn_2O_4$ nanofibres were fabricated from a mixture of metal acetates and poly(vinylpyrrolidone) (PVP) in N,N-dimethylformamide (DMF) by an electrospinning technique combined with a post-heat-treatment process. For simplicity, the $MnCo_2O_4$ and $CoMn_2O_4$ nanofibres will hereafter be referred to as MCO-NF and CMO-NF, respectively. Morphological and structural characteristics of MCO-NF and CMO-NF were examined using various tools, such as scanning electron microscopy (SEM), energy-dispersive X-ray spectroscopy (EDS), X-ray diffractometry (XRD), and transmission electron microscopy (TEM). Figures 1a and b display low-magnification SEM images of MCO-NF and CMO-NF, respectively. Both of the samples show typical fibrous morphologies with lengths of several hundred micrometers and diameters of 140–200 nm. All of the fibres have particulate surfaces, as shown in the high-magnification SEM micrographs in Fig. 1c and d. CMO-NF has a rougher surface than MCO-NF, and nano-sized pores (30–70 nm in size) are observed locally, as indicated by the arrows in Fig. 1d. The EDS mapping analysis (Fig. 1e and f) reveals that overall the fibres have uniform elemental distributions; however, the possibility of local segregations of the cationic elements such as Co and Mn cannot be ruled out. The ratio of Mn to Co was estimated to be ~0.50 for MCO-NF and ~1.93 for CMO-NF.

Figures 2a and b present the XRD patterns of MCO-NF and CMO-NF, respectively. All the reflections of MCO-NF (Fig. 2a) could be assigned to a face-centred-cubic spinel $MnCo_2O_4$ phase (space group Fd3m (227), JCPDS No. 23-1237), while CMO-NF (Fig. 2b) is found to consist of a body-centred tetragonal spinel $CoMn_2O_4$ phase (space group I4$_1$/amd, JCPDS No. 77-0471). No noticeable impurity phases were detected from the samples. More detailed structural information was acquired by TEM observation (Fig. 3). As shown in Fig. 3a and b, MCO-NF and CMO-NF have polygonal-shaped crystallites with sizes of 15–30 nm and 20–48 nm, respectively, and they feature a porous morphology, which is confirmed by the locally existing bright contrast regions among the dark contrast regions within the fibres. Figures 3c and d show high-resolution (HR) TEM images of the square areas marked in Fig. 3a and b, respectively. The corresponding fast-Fourier transform (FFT) patterns are also given in the respective insets. The interplanar spacing (d) of the lattice fringes in the MCO-NF crystal (Fig. 3c) was determined to be ~0.25 nm, and it was assigned to the (311) plane of the cubic spinel $MnCo_2O_4$ phase. For CMO-NF (Fig. 3d), lattice fringes corresponding to the (011) and (101) planes of the tetragonal spinel $CoMn_2O_4$ phase are observed. These findings are in accordance with the XRD results of Fig. 2. N_2 adsorption-desorption isotherm measurements (data not shown) revealed that both of the samples have a mesoporous structure characterised by a type IV isotherm with a type H1 hysteresis loop[30]. The

average pore size and total pore volume of MCO-NF were 21.1 nm and 0.102 cm^3 g^{-1}, respectively. The CMO-NF sample had an average pore size of 19.4 nm and a total pore volume of 0.078 cm^3 g^{-1}. The Brunauer−Emmett−Teller (BET) surface areas of MCO-NF and CMO-NF were estimated to be 19.3 m^2 g^{-1} and 16.0 m^2 g^{-1}, respectively. According to the BET analysis, MCO-NF exhibits a slightly more porous characteristic than CMO-NF, which indicates the presence of a relatively large amount of mesopores in MCO-NF.

Electrocatalytic activities of 1D $MnCo_2O_4$ and $CoMn_2O_4$ nanofibres towards oxygen reduction and evolution. Prior to application of MCO-NF and CMO-NF as cathode catalysts for rechargeable metal-air batteries, we examined the capability of MCO-NF and CMO-NF to catalyse the ORR and OER by rotating disc electrode (RDE) experiments. MCO-NF or CMO-NF was mixed with carbon black (used as a conducting agent) to prepare MCO-NF/C or CMO-NF/C, respectively, and then the mixture was uniformly coated onto an RDE electrode. Figure 4a illustrates the cathodic polarisation (measured disc current *vs.* applied disc potential) curves for the ORR in 0.1 M KOH. The results demonstrate that MCO-NF and CMO-NF play a substantial role in facilitating electrochemical oxygen reduction in an alkaline electrolyte. The oxygen reduction on NCO-NF/C and CMO-NF/C starts at higher potentials, and the reduction currents are much higher at a given potential than those of the catalyst-free carbon. In addition, we note that MCO-NF with a cubic spinel structure exhibits higher onset and half-wave potentials compared to the tetragonal spinel CMO-NF, indicating the better ORR properties of MCO-NF.

The electrochemical oxygen reduction should proceed *via* a four-electron transfer pathway, *i.e.*, direct reduction of O_2 to OH^- ($O_2 + 2H_2O + 4e^- \rightarrow 4OH^-$), which is more oxygen-efficient than a two-electron transfer pathway ($O_2 + H_2O + 2e^- \rightarrow HO_2^- + OH^-$)[31]. To determine the ORR pathway, the number of electrons (n) exchanged during the ORR was calculated from the well-known Koutechky-Levich (K-L) equation[32]. The origins for different behaviours of MCO-NF/C and CMO-NF/C in the purely diffusion-controlled region (< 0.57 V *vs.* RHE) have not been understood yet. We speculate that such a difference possibly originates from slightly different microstructures of the two RDE electrodes made of MCO-NF and CMO-NF. To avoid this problem, therefore, the n values were estimated at 0.6 V *vs.* RHE in which no drastic change in the polarization curves was observed for CMO-NF/C. The cathodic polarisation curves were first measured at various rotation rates of 200–2,500 rpm, and the value of n was then estimated from the slope of the current^{-1} *vs.* rotation rate$^{-1/2}$ curve, as shown in Fig. 4b. The value of n for the catalyst-free carbon was calculated to be ~2.1, which indicates that the two-electron transfer reaction is dominant for the ORR on carbon. On the other hand, the values of n for MCO-NF/C and CMO-NF/C were estimated to be ~3.9 and ~3.7, respectively, suggesting that MCO-NF and CMO-NF cause the ORR to proceed by the four-electron transfer reaction. According to the previous studies on the oxide/carbon composite catalysts reported by Li *et al.*[33] and Sunarso *et al.*[34], the n values close to 4 for MCO-NF/C and CMO-NF/C may be understood as follows: O_2 is reduced to HO_2^- on carbon *via* the two-electron transfer reaction. Then, HO_2^- species generated on carbon would undergo another two-electron transfer for further reduction to OH^- on the highly active spinel oxide adjacent to carbon, thereby leading to $n \approx 4$ (*i.e.*, so-called the two + two electron transfer process)[33,34]. In parallel, O_2 is directly reduced to OH^- on the spinel oxide (MCO-NF or CMO-NF) *via* the four-electron transfer reaction.

In addition to the requirement of high ORR activity, catalytic materials for rechargeable metal-air batteries should be able to effectively catalyse electrochemical oxygen evolution, which is of particular importance for reducing the charge voltages of batteries and for improving their round-trip efficiency. The OER activity was
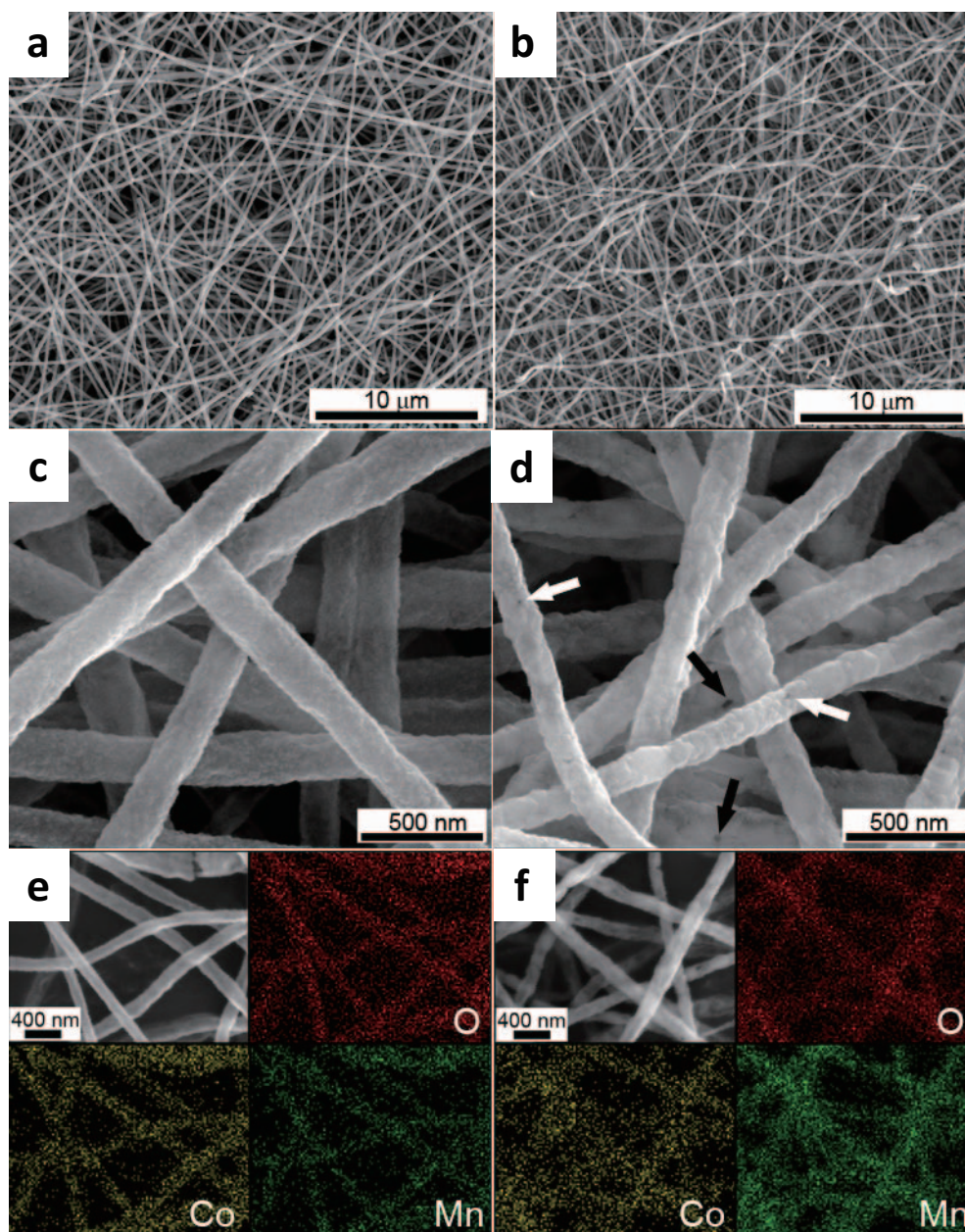
Figure 1 | Morphological and elemental analyses of the electrospun nanofibres of MnCo₂O₄ (MCO-NF) and CoMn₂O₄ (CMO-NF). (a–d) SEM micrographs and (e, f) EDS mapping data of (a, c, e) MCO-NF and (b, d, f) CMO-NF. In (d), the arrows indicate pores present on the fibre surfaces. (e) and (f) present the elemental distributions of O, Co, and Mn for the corresponding SEM images.

evaluated from the anodic polarisation curves measured during a potential sweep from open circuit potentials (OCPs) to 1.7 V *vs.* reversible hydrogen electrode (RHE) (Fig. 4c). The catalyst-free carbon exhibits an oxidation current as low as 0.079 mA at 1.6 V *vs.* RHE. Both MCO-NF/C and CMO-NF/C show considerably higher activity towards the OER as compared with carbon, namely, more than two-fold improvements in the oxidation current at 1.6 V *vs.* RHE. It should be noted that the anodic currents in Fig. 4c contain the currents for the parasitic oxidation reactions of carbon in the electrode and of other species in the electrolyte, which implies that the Faradaic efficiency is lower than 100%. Given the fact that the experiments were performed under the same conditions (including the electrode and electrolyte preparations), we believe that the anodic polarization curves in Fig. 4c indicate the remarkably improved OER activities of MCO-NF/C and CMO-NF compared to carbon. It is also interesting to note that the tetragonal spinel CMO-NF delivers

slightly higher oxidation currents than the cubic spinel MCO-NF over the whole potential range, which is in contrast with the trend observed for the ORR (Fig. 4a). In Supplementary Table S1, the mass and specific activities of the spinel oxide catalysts for the ORR and OER developed in this work were compared with those of various oxide catalysts reported in the literature.

Electrochemical performance of rechargeable Zn-air batteries with 1D fibrous MnCo₂O₄ and CoMn₂O₄ catalysts. The strong bi-functionality of the MCO-NF and CMO-NF catalysts towards the ORR and OER was clearly demonstrated from the RDE experiments (Fig. 4). As a next step, we constructed Zn-air batteries using MCO-NF and CMO-NF as cathode catalysts and tested their electrochemical performance under realistic operating conditions. The coin-type battery consisted of a metallic Zn anode, 6 M KOH electrolyte, and the MCO-NF/C or CMO-
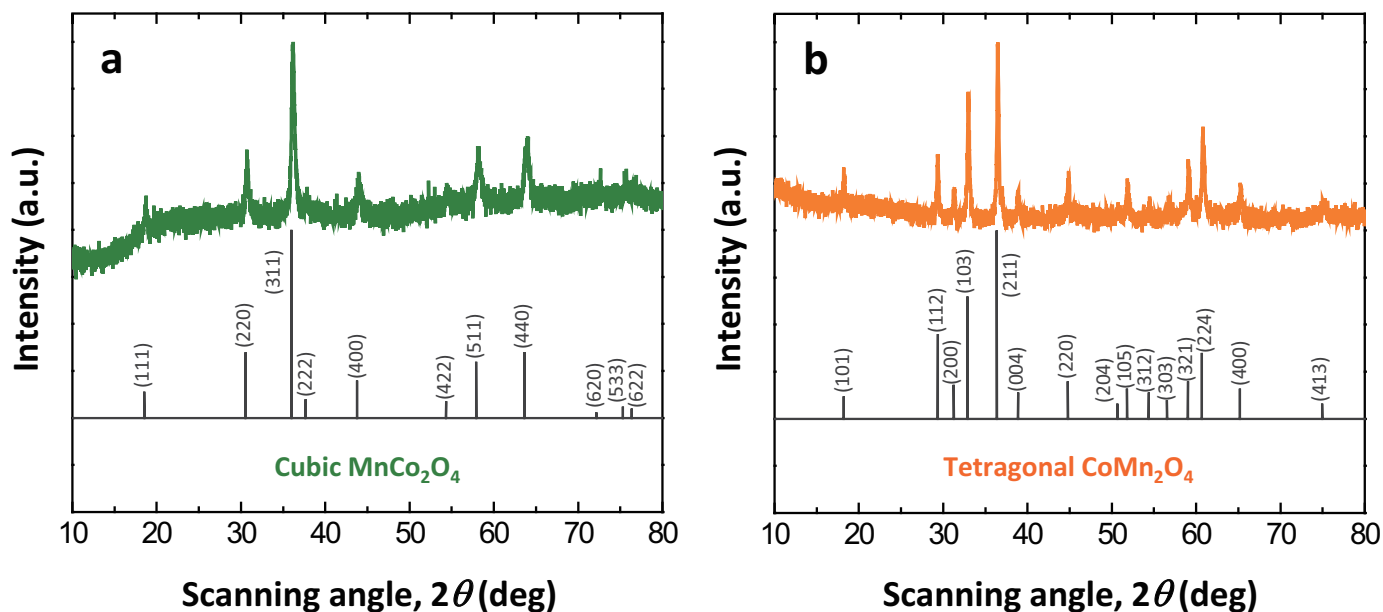
Figure 2 | Structural characterisation of the electrospun nanofibres of MnCo₂O₄ (MCO-NF) and CoMn₂O₄ (CMO-NF). XRD patterns of (a) MCO-NF and (b) CMO-NF. The reference XRD patterns for cubic $MnCo_2O_4$ (JCPDS No. 23-1237) and tetragonal $CoMn_2O_4$ (JCPDS No. 77-0471) phases are presented in (a) and (b), respectively.
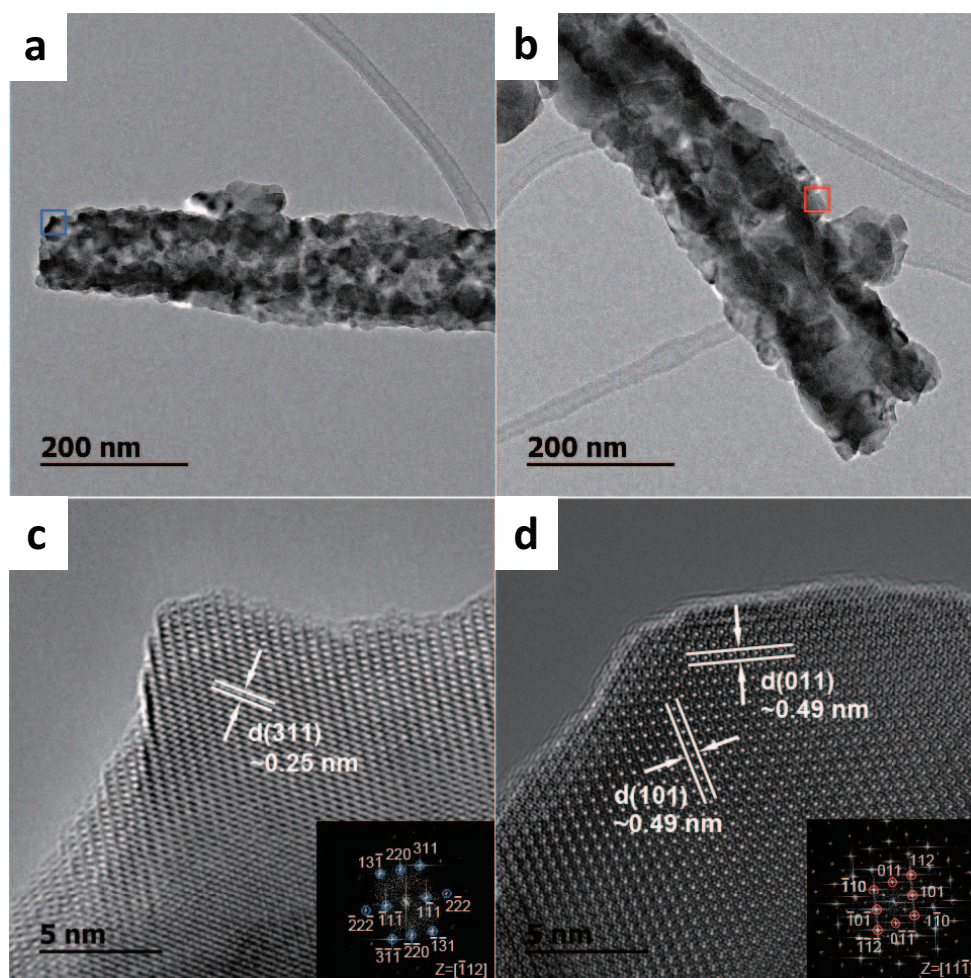
Figure 3 | TEM analysis of the electrospun nanofibres of MnCo₂O₄ (MCO-NF) and CoMn₂O₄ (CMO-NF). (a, b) Low-magnification TEM images of (a) MCO-NF and (b) CMO-NF. (c, d) HRTEM images of the regions marked by squares in (a) and (b). The insets in (c) and (d) display the corresponding FFT patterns with the zone axes of [$\bar{1}12$] and [$11\bar{1}$], respectively.
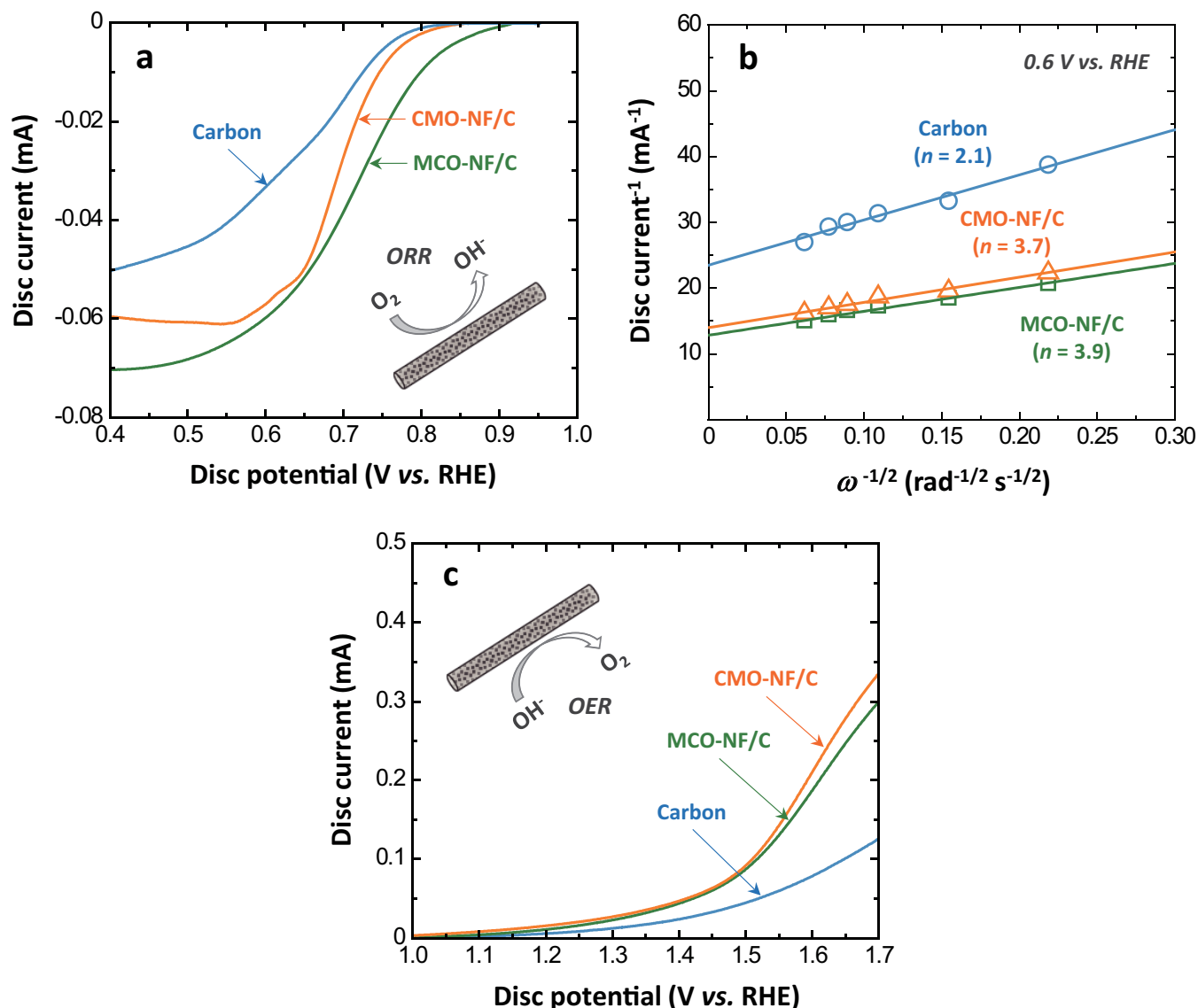
Figure 4 | Electrocatalytic activity of the electrospun nanofibres of MnCo$_2$O$_4$ (MCO-NF) and CoMn$_2$O$_4$ (CMO-NF) towards the ORR and OER.
(a) Cathodic polarisation curves for the ORR measured at a rotation rate of 1,200 rpm, and (b) Koutechky-Levich plots at 0.6 V vs. RHE, constructed by using the cathodic polarisation curves collected at various rotation rates (ω). (c) Anodic polarisation curves for the OER. The RDE measurements were performed in 0.1 M KOH using a potential scan rate of 10 mV s^{-1}. For comparison, the data obtained for the catalyst-free carbon are included.

NF/C cathode (open to the ambient air). Typically, the Zn-air battery assembled in this work delivered a capacity as high as 125 mAh upon full discharging at 10 mA cm^{-2} (Supplementary Fig. S1). All of the battery tests were performed using the ambient air. The ORR-OER kinetics on the cathode (air electrode) should have a major impact on the discharge-charge overpotentials of a Zn-air battery rather than on its discharge capacity. Note that, in principle, the total battery capacity is exclusively determined by the amount of Zn to be oxidised, as long as oxygen is continuously supplied from the atmosphere. For this reason, in this work, the main focus of the battery tests was on characterising the effect of the fibrous spinel oxide catalysts on the overpotentials for discharge and charge, i.e., discharge-charge voltage gaps or round-trip efficiency.

Figures 5a and b present the discharge-charge profiles of the Zn-air batteries having the MCO-NF and CMO-NF catalysts in their cathodes measured at constant current densities of 10 mA cm^{-2} and 25 mA cm^{-2}, respectively (see Supplementary Fig. S2 for the data reproducibility). The same experiments were con-

ducted using the catalyst-free carbon and commercial carbon-supported Pt (20 wt.% Pt) (denoted as Pt/C) cathodes, and the results are included in Fig. 5a and b. When the battery was discharged (or charged) with a constant current, the battery voltage decreased (or increased) with increasing time, and then it quickly reached a steady-state value within several tens of seconds. The steady-state voltages for discharge and charge vary strongly with the catalyst used in the cathode. Figure 5c illustrates the discharge and charge voltages of the Zn-air batteries as a function of the applied current density for the various cathodes: carbon, MCO-NF/C, CMO-NF/C, and Pt/C. In comparison with the catalyst-free carbon cathode, the MCO-NF and CMO-NF catalysts significantly reduce the discharge-charge voltage gaps over the whole current range. This result can be understood from the RDE data (Fig. 4) that demonstrated the appreciable bi-functional activity towards the ORR and OER. The voltage gaps of MCO-NF/C and CMO-NF/C were determined to be 1.23 V and 1.24 V at 50 mA cm^{-2}, which were smaller by ~440 mV compared to the catalyst-free carbon cathode. While the commercial Pt/C cathode leads to the smallest

discharge overpotentials of the Zn-air battery, the MCO-NF/C and CMO-NF/C cathodes outperform Pt/C upon battery charging. Consequently, the voltage gaps for the MCO-NF/C and CMO-NF/C cathodes were determined to be smaller than that of the Pt/C cathode (1.27 V). To determine the contributions of Zn stripping and plating to the total discharge and charge overpotentials of the Zn-air battery, respectively, we constructed a Zn symmetric cell (Zn/6 M KOH/Zn) and measured the galvanostatic potential transient curves by applying various current densities of 1 mA cm^{-2} to 50 mA cm^{-2} (Supplementary Fig. S3). The voltage gaps for Zn stripping and plating were measured to be 1.5–59.4 mV at 1–50 mA cm^{-2}, respectively, that is, at most 0.3~5.1% of the total battery voltage gaps. The rechargeability of the Zn-air batteries was tested with the MCO-NF and CMO-NF catalysts, and the resulting discharge-charge profiles obtained during consecutive cycles are shown in Fig. 5d. It is clearly seen that the batteries having the fibrous spinel oxide catalysts exhibit more stable cycling performance with smaller voltage gaps compared to the catalyst-free carbon cathode.

Discussion

The RDE experiments (Fig. 4) and battery tests (Fig. 5) demonstrated that MCO-NF and CMO-NF have an outstanding ability to catalyse both the ORR and the OER in an alkaline electrolyte, and thus, they can function as efficient bi-functional catalysts for rechargeable Zn-air batteries, leading to reduced voltage gaps (improved round-trip efficiency). It should be pointed out that the voltage gaps of the Zn-air batteries with MCO-NF and CMO-NF were smaller than that of the battery with Pt/C. Pt is still considered the best ORR catalyst, but its surface is susceptible to passivation with oxide layers when exposed at high potentials, resulting in loss of the OER activity[5]. On the other hand, the MCO-NF and CMO-NF catalysts play an active role in reducing the battery voltages upon charging, as proved in our battery tests (Fig. 5). The promising bi-functional catalytic properties of MCO-NF and CMO-NF can be attributed to their unique electronic and morphological characteristics: (1) MCO and CMO have relatively low activation energies for electron transfer between cations with different valence states, and hence, they are able to offer donor-acceptor chemisorption sites for oxygen
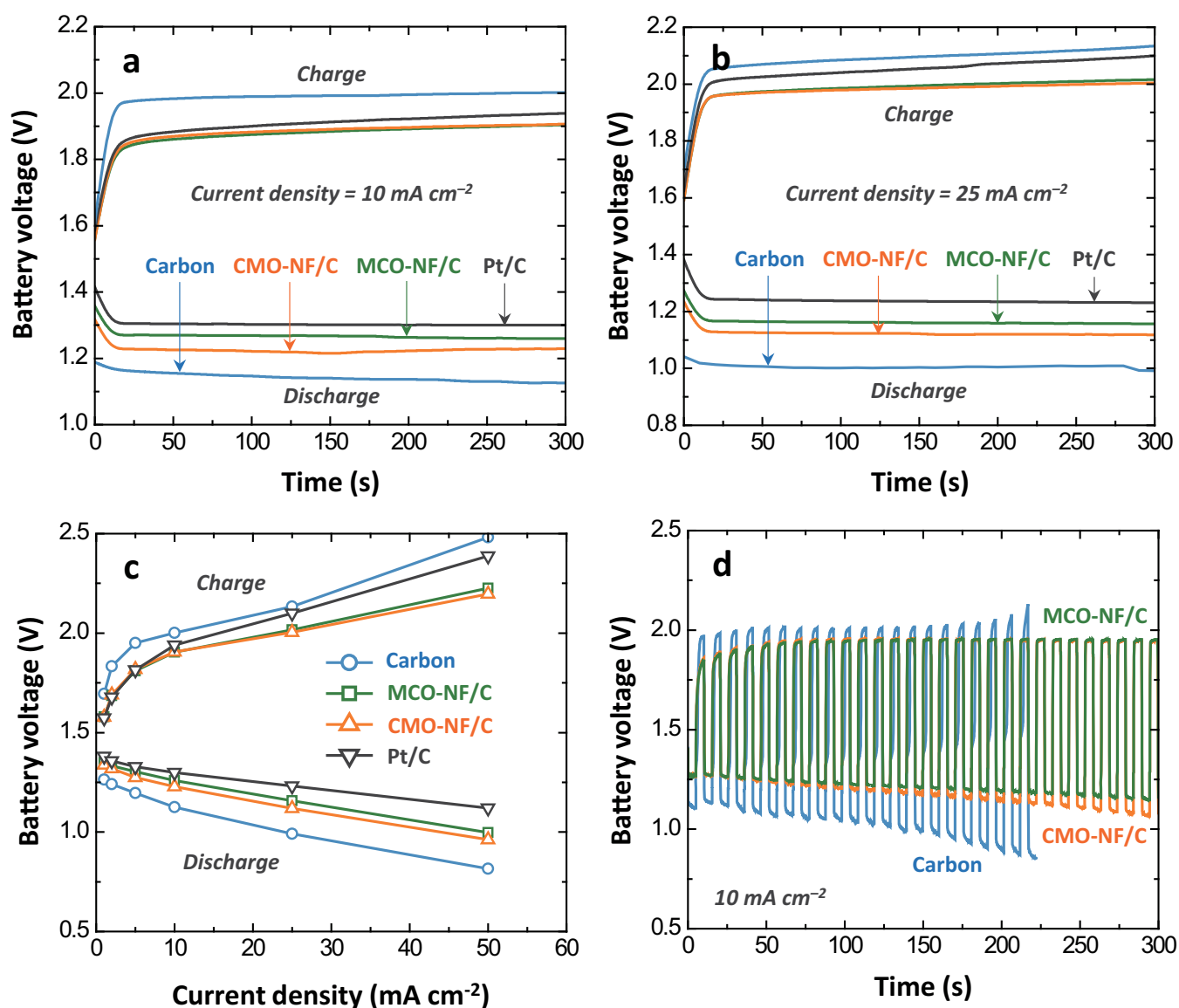
Figure 5 | Electrochemical performance of Zn-air batteries assembled using the fibrous MnCo$_2$O$_4$ (MCO-NF) and CoMn$_2$O$_4$ (CMO-NF) catalysts. (a, b) Galvanostatic discharge-charge curves measured at (a) 10 mA cm^{-2} and (b) 25 mA cm^{-2}. (c) Battery voltages measured at various current densities. (d) Cycling performance at 10 mA cm^{-2}. The batteries contained a metallic Zn anode and 6 M KOH. For comparison, the data measured for the catalyst-free carbon and Pt/C cathodes are included.

molecules during the ORR and OER[18,35]. (2) The MCO-NF and CMO-NF catalysts provide a large number of active reaction sites and facilitate mass transport through their porous 1D structure.

In Fig. 4 and 5, we observed slightly different catalytic behaviour between MCO-NF and CMO-NF, that is to say, higher ORR activity on MCO-NF, but higher OER activity on CMO-NF. Taking into account that the surface areas of the two materials are almost the same, it would be reasonable to explain such a difference in the ORR-OER activity in terms of the cation composition and crystal structure. Rios *et al.*[35] reported that the ORR activity of cubic spinel $Mn_xCo_{3-x}O_4$ $(0 < x < 1)$ increases with increasing Mn content, partly due to an increased number of the Mn redox couples responsible for catalysing the ORR. In contrast, the higher the Mn concentration, the lower the OER activity is, because Mn species strongly inhibit the surface OH$^-$ oxidation that would be the rate-determining step for the OER. Moreover, from an atomic simulation study of the Co-Mn-O spinel system, Cheng *et al.*[36] predicted that the surface of the cubic spinel can provide more stable transition metal-adsorbed O_2 bonds as well as a larger number of active sites as compared to the tetragonal spinel. Therefore, the cubic spinel surface would generally show enhanced ORR activity compared to the tetragonal spinel. The OER activity was predicted to be lower for the cubic spinel, based on the assumption that the OER is the reverse process of the ORR. These results are in accord with our experimental finding that the ORR activity of the cubic spinel MCO-NF is higher than that of the tetragonal spinel CMO-NF, whereas the OER activity of the former is lower.

The efficacy of the MCO-NF and CMO-NF catalysts in Zn-air batteries has been proved experimentally, but their stability is of potential concern. In fact, the cycling tests of the batteries with MCO-NF and CMO-NF (Fig. 5d) exhibited the signs of performance decay, *i.e.*, an increasing voltage gap with increasing cycles. The possible origins of the increased voltage gaps include the degradation of the catalyst-containing cathode. The cathode stability was independently investigated using a three-electrode half-cell composed of 6 M KOH electrolyte, an Hg/HgO reference electrode, and a Pt counter electrode. This allows us to avoid complications arising from the Zn degradation and to gain more useful information on the cathode stability. The MCO-NF/C and CMO-NF/C cathodes were subjected to an "accelerated" potential cycling test with a scan rate of 50 mV s^{-1} in the range of 0.22–1.62 V *vs.* RHE, and then the structural properties of the cycled cathodes were examined by using XRD and X-ray photoelectron spectroscopy (XPS).

Figures 6a and b present XRD patterns of the MCO-NF/C and CMO-NF/C cathodes, respectively, obtained before and after the stability tests for 500 cycles. All the diffraction peaks due to the cubic or tetragonal spinel phase are clearly seen, even after 500 cycles. The additional peaks (designated by +) correspond to potassium carbonates formed as a result of the parasitic reaction between KOH and atmospheric CO_2[5]. This confirms that the crystal structures of the MCO-NF and CMO-NF catalysts remain unchanged over the course of repeated discharge-charge cycling. The surface oxidation states of the cycled MCO-NF and CMO-NF catalysts were further investigated by XPS, as shown in Fig. 6c and d. The Co 2p spectra can be well fitted by considering the spin-orbit doublet characteristics of Co^{2+} and Co^{3+} with satellite peaks, while the two main peaks for Mn $2p_{3/2}$ and Mn $2p_{1/2}$ for Mn 2p spectra can be deconvoluted into the characteristic curves of Mn^{2+} and Mn^{3+} [37,38]. The XPS analysis further confirms that the stability tests for 500 cycles caused no serious damage to the MCO-NF and CMO-NF catalysts, except for a slight increase in the relative concentration of Mn^{3+} and Co^{3+} ions.

Having noticed more serious degradation of the catalyst-free carbon cathode from Fig. 5d, we have paid attention to possible structural changes in the carbon mixed with the catalysts. Figure 7 shows typical cyclic voltammograms of carbon (without any catalysts) measured on the RDE in 1 M KOH at a scan rate of 50 mV s^{-1} for 100 cycles. During consecutive potential cycling, both the anodic OER and cathodic ORR currents decreased drastically with increasing cycles. After 50 cycles, the anodic current became negligibly small, and the cathodic half-wave potential was negatively shifted. From the N_2 adsorption-desorption isotherms of the pristine and cycled carbon cathodes (the inset in Fig. 7), we found that the BET surface area and total pore volume of the cathode were remarkably reduced from 125.9 m^2 g^{-1} and 0.283 cm^3 g^{-1} to 29.9 m^2 g^{-1} and 0.149 cm^3 g^{-1}, respectively. This clearly indicates the carbon loss as well as the collapse of porous structures, primarily due to carbon oxidation at the high potentials pertinent to OER[5,13]. Given the fact that the MCO-NF and CMO-NF catalysts have sufficient stability, as revealed by the accelerated cycling tests combined with the XRD and XPS analyses, we believe that the observed performance degradation of the Zn-air battery (Fig. 5d) is mainly attributable to carbon corrosion, which can lead to loss of the structural integrity and electronic conducting paths of the cathode.

In summary, we successfully fabricated 1D fibrous oxide (MCO-NF and CMO-NF) catalysts by an electrospinning technique combined with a post-heat-treatment process. The RDE experiments and battery tests indicate that the spinel oxide nanofibre catalysts have strong bi-functionality, enabling them to promote the ORR and OER in an alkaline electrolyte, and hence, they greatly reduced the discharge-charge voltage gaps (improve the round-trip efficiency) of the Zn-air batteries. The unique structure of the MCO-NF and CMO-NF catalysts seems to have a beneficial role in improving the electrochemical properties by providing a large number of active reaction sites and by facilitating mass transport through the porous 1D structure. Furthermore, we found that the MCO-NF and CMO-NF catalysts remained stable during the accelerated cycling tests; however, the carbon corrosion in the cathode brings about performance degradation of the Zn-air battery on cycling. Carbon has been commonly used as a conducting agent and/or a catalyst support in most of the cathodes for metal-air batteries. Future research should be devoted to developing bi-functional cathodes that can warrant stable cycling operations without concerns about carbon oxidation at high potentials.

Methods

Synthesis of $MnCo_2O_4$ and $CoMn_2O_4$ nanofibres. Porous $MnCo_2O_4$ and $CoMn_2O_4$ fibres were fabricated by an electrospinning method. In a typical synthesis of $MnCo_2O_4$ fibres, the electrospinning solution was prepared by dissolving 3 mmol manganese acetate tetrahydrate (Mn(CH$_3$COO)$_2$·4H$_2$O, 99%, Aldrich) and 6 mmol cobalt acetate tetrahydrate (Co(CH$_3$COO)$_2$·4H$_2$O, 99%, Aldrich) powders in 10 mL N,N-dimethylformamide (99%, Aldrich) solvent under magnetic stirring for 1 h. 1.3 g poly(vinylpyrrolidone) (PVP, (C$_6$H$_9$NO)$_n$, M$_w$~1,300,000, Aldrich) powder was then added into the solution and uniformly mixed for 1 h. In the case of $CoMn_2O_4$ fibres, 3 mmol cobalt acetate tetrahydrate and 6 mmol manganese acetate tetrahydrate powders were used to make the solution. The transparent spinning solutions were immediately put into a plastic syringe attached to a 23 gauge needle that was electrically connected to a high voltage power supply. The solutions were then subjected to electrospinning onto an Al-foil-wrapped drum collector using a DC voltage of 25 kV and a feeding rate of 1.2 mL h^{-1}. The distance between the needle tip and the drum collector was 15 cm. The electrospun fibres were carefully detached from the collector, then dried at 150°C for 3 h in an oven to vaporise the residual solvent, and finally heat-treated at 600°C for 3 h in air.

Materials characterisation. The morphologies and microstructures of the synthesized fibres were analysed by field-emission (FE) SEM (JEOL JSM-7000F) and TEM (JEM-2100F, Japan Electronic Optics Ltd.). The elemental distribution was examined by EDS attached to the SEM instrument. The phases and crystal structures were investigated by XRD (Empyrean, PAN analytical) with Cu-$K\alpha$ radiation (λ = 1.54056 Å) and FFT patterns. N_2 sorption isotherms were measured by a surface area and porosimetry analyser (TristarII 3020, Micromeritics). The specific surface area and pore volume were estimated by BET and Barrett-Joyner-Halenda (BJH) methods, respectively. XPS measurements were performed on a Thermo MultiLab 2000 system with a monochromatic Al $K\alpha$ X-ray source.

Electrochemical experiments. To evaluate the electrocatalytic activity, rotating disc electrode (RDE) experiments were carried out in a three-electrode electrochemical cell using a potentiostat (CH Instruments). To prepare the catalyst ink[39], the conductive carbon (Vulcan XC72R, Cabot, USA, 50 wt.%) and catalyst (50 wt.%) were
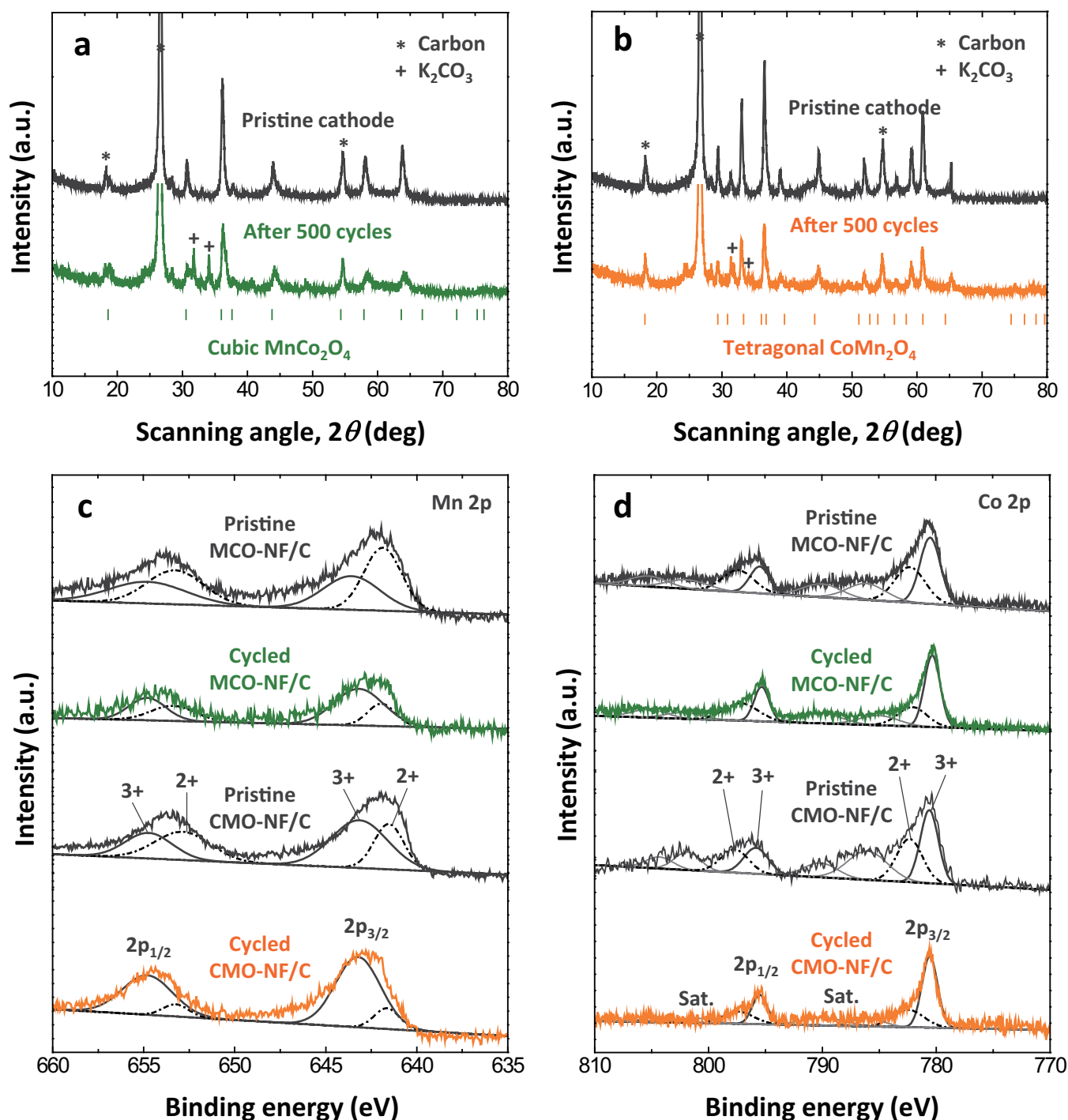
Figure 6 | XRD and XPS analyses of the pristine and cycled cathodes consisting of the fibrous spinel oxide catalysts and carbon. (a, b) XRD patterns of the (a) MCO-NF/C and (b) CMO-NF/C cathodes obtained before and after the accelerated cycling test. (c, d) XPS spectra in (c) Mn 2p and (d) Co 2p regions of the pristine and cycled MCO-NF/C and CMO-NF/C cathodes.

homogeneously dispersed by ultrasonication. The resultant suspension was dropped onto the polished glassy carbon disc (3 mm in diameter) with 15 μg of loading. After drying, 5 μg of Nafion solution was coated onto the catalyst layer to give it good adhesion with the RDE. A Pt wire and Ag/AgCl electrode served as the counter and reference electrodes, respectively. The electrolyte was 0.1 M KOH. All potentials reported in this work are referred to a reversible hydrogen electrode (RHE). The linear sweep voltammograms were obtained by scanning the potential from the OCP to 0.4 V *vs.* RHE for the ORR and from the OCP to 1.7 V *vs.* RHE for the OER at a scan rate of 10 mV s^{-1}. Throughout the RDE experiments, high-purity O_2 gas was purged into the electrolyte to maintain the O_2-saturated condition. In particular, the ORR currents were corrected by the background currents measured in the N_2-saturated electrolyte.

A 2032 coin-type cell having a cathode open to the ambient air was used for the electrochemical tests of the Zn-air battery. The Zn-air battery was made of a gelled Zn anode, a separator (Celgard 3501) impregnated with 6 M KOH, and the composite cathode. For the cathode preparation, a composite powder of the catalyst (20 wt.%) and conductive carbon (75 wt.%) was homogeneously mixed with 5 wt.% poly(tetrafluoroethylene) (PTFE) binder in ethanol. Then, the cathode was finally fabricated by pressing the composite sheet with a twin roller and drying it under vacuum at 60°C overnight. The diameter of the cathode was 1.0 cm (geometric area = 0.785 cm²). The electrode loading was ~25 mg cm^{-2}. The gelled Zn anode was prepared by mixing metallic Zn powder (Alfa Aesar) with a polyacrylic acid gelling agent (Aldrich) in 6 M KOH. The gelled Zn anode contained 80 wt.% Zn, 0.5 wt.% gelling agent, and 19.5 wt.% KOH solution. The Zn-air battery was galvanostatically dis-
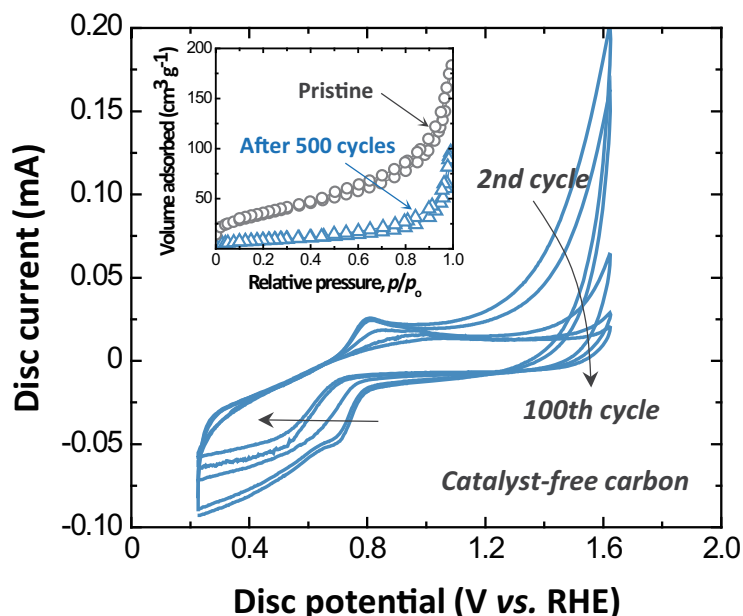
Figure 7 | Cyclic voltammograms of the catalyst-free carbon measured in 1 M KOH using the RDE at a scan rate of 50 mV s⁻¹ and a rotation rate of 1,600 rpm. The inset presents the N_2 adsorption-desorption isotherms of the pristine and cycled carbon cathodes.

charged and charged at room temperature with a Maccor Series 4000. All of the battery tests were performed using the ambient air. The accelerated cycling tests on the cathode materials were performed using a three-electrode half-cell. A Pt wire and an Hg/HgO electrode were used as the counter and reference electrodes, respectively. The composite cathode was subjected to a potential cycling test with a scan rate of 50 mV s⁻¹ in the potential range of 0.22 to 1.62 V *vs.* RHE in 6 M KOH.

1. Armand, M. & Tarascon, J.-M. Building better batteries. *Nature* **451**, 652–657 (2008).
2. Neburchilov, V., Wang, H., Martin, J. J. & Qu, W. A review on air cathodes for zinc-air fuel cells. *J. Power Sources* **195**, 1271–1291 (2010).
3. Girishkumar, G., McCloskey, B., Luntz, A. C., Swanson, S. & Wilcke, W. Lithium-air battery: promise and challenges. *J. Phys. Chem. Lett.* **1**, 2193–2203 (2010).
4. Cheng, F. & Chen, J. Metal-air batteries: from oxygen reduction electrochemistry to cathode catalysts. *Chem. Soc. Rev.* **41**, 2172–2192 (2012).
5. Li, Y. & Dai, H. Recent advances in zinc-air batteries. *Chem. Soc. Rev.* **43**, 5257–5275 (2014).
6. Xu, Y., Ruban, A. V. & Mavrikakis, M. Adsorption and dissociation of O_2 on Pt-Co and Pt-Fe alloys. *J. Am. Chem. Soc.* **126**, 4717–4725 (2004).
7. Wang, C., Daimon, H., Lee, Y., Kim, J. & Sun, S. Synthesis of monodisperse Pt nanocubes and their enhanced catalysis for oxygen reduction. *J. Am. Chem. Soc.* **129**, 6974–6975 (2007).
8. Spendelow, J. S. & Wieckowski, A. Electrocatalysis of oxygen reduction and small alcohol oxidation in alkaline media. *Phys. Chem. Chem. Phys.* **9**, 2654–2675 (2007).
9. Suntivich, J., May, K. J., Gasteiger, H. A., Goodenough, J. B. & Shao-Horn, Y. A perovskite oxide optimized for oxygen evolution catalysis from molecular orbital principles. *Science* **334**, 1383–1385 (2011).
10. Wang, L. *et al.* CoMn₂O₄ spinel nanoparticles grown on graphene as bifunctional catalyst for lithium-air batteries. *J. Electrochem. Soc.* **158**, A1379–A1382 (2011).
11. Malkhandi, S. *et al.* Electrocatalytic properties of nanocrystalline calcium-doped lanthanum cobalt oxide for bifunctional oxygen electrodes. *J. Phys. Chem. Lett.* **3**, 967–972 (2012).
12. Liang, Y. *et al.* Covalent hybrid of spinel manganese-cobalt oxide and graphene as advanced oxygen reduction electrocatalysts. *J. Am. Chem. Soc.* **134**, 3517–3523 (2012).
13. Chen, Z. *et al.* Highly active and durable core-corona structured bifunctional catalyst for rechargeable metal-air battery application. *Nano Lett.* **12**, 1946–1952 (2012).
14. Lee, D. U., Kim, B. J. & Chen, Z. One-pot synthesis of a mesoporous NiCo₂O₄ nanoplatelet and graphene hybrid and its oxygen reduction and evolution activities as an efficient bi-functional electrocatalyst. *J. Mater. Chem. A* **1**, 4754–4762 (2013).
15. Ryu, W.-H. *et al.* Bifunctional composite catalysts using Co₃O₄ nanofibers immobilized on nonoxidized graphene nanoflakes for high-capacity and long-cycle Li-O₂ batteries. *Nano Lett.* **13**, 4190–4197 (2013).
16. Jung, K.-N. *et al.* Urchin-like α-MnO₂ decorated with Au and Pd as a bi-functional catalyst for rechargeable lithium-oxygen batteries. *J. Power Sources* **244**, 328–335 (2013).
17. Jung, K.-N. *et al.* Doped lanthanum nickelates with a layered perovskite structure as bifunctional cathode catalysts for rechargeable metal-air batteries. *ACS Appl. Mater. Interfaces* **5**, 9902–9907 (2013).
18. Prabu, M., Ketpang, K. & Shanmugam, S. Hierarchical nanostructured NiCo₂O₄ as an efficient bifunctional non-precious metal catalyst for rechargeable zinc-air batteries. *Nanoscale* **6**, 3173–3181 (2014).
19. Shui, J.-L., Karan, N. K., Balasubramanian, M., Li, S.-Y. & Liu, D.-J. Fe/N/C composite in Li-O₂ battery: studies of catalytic structure and activity toward oxygen evolution reaction. *J. Am. Chem. Soc.* **134**, 16654–16661 (2012).
20. Wang, S. *et al.* Oxygen-enriched carbon material for catalyzing oxygen reduction towards hybrid electrolyte Li-air battery. *J. Mater. Chem.* **22**, 21051–21056 (2012).
21. Yang, Z. *et al.* Sulfur-doped graphene as an efficient metal-free cathode catalyst for oxygen reduction. *ACS Nano* **6**, 205–211 (2012).
22. Park, H. W. *et al.* Bi-functional N-doped CNT/graphene composite as highly active and durable electrocatalyst for metal air battery applications. *J. Electrochem. Soc.* **160**, A2244–A2250 (2013).
23. Li, Q., Cao, R., Cho, J. & Wu, G. Nanostructured carbon-based cathode catalysts for nonaqueous lithium–oxygen batteries. *Phys. Chem. Chem. Phys.* **16**, 13568–13582 (2014).
24. Yoo, E. & Zhou, H. Hybrid electrolyte Li-air rechargeable batteries based on nitrogen- and phosphorus-doped graphene nanosheets. *RSC Adv.* **4**, 13119–13122 (2014).
25. Jeong, G. *et al.* Core-shell structured silicon nanoparticles@TiO₂₋ₓ/carbon mesoporous microfiber composite as a safe and high-performance lithium-ion battery anode. *ACS Nano* **8**, 2977–2985 (2014).
26. Kim, J.-G. *et al.* Zr⁴⁺ doping in Li₄Ti₅O₁₂ anode for lithium-ion batteries: open Li⁺ diffusion paths through structural imperfection. *ChemSusChem* **7**, 1451–1457 (2014).
27. Michailovski, A. *et al.* Studying the solvothermal formation of MoO₃ fibers by complementary in situ EXAFS/EDXRD techniques. *Angew. Chem. Int. Ed.* **44**, 5643–5647 (2005).
28. Bae, C. *et al.* Template-directed synthesis of oxide nanotubes: fabrication, characterization, and applications. *Chem. Mater.* **20**, 756–767 (2008).
29. Hartgerink, J. D., Beniash, E. & Stupp, S. I. Self-assembly and mineralization of peptide-amphiphile nanofibers. *Science* **294**, 1684–1688 (2001).
30. Kruk, M. & Jaroniec, M. Gas adsorption characterization of ordered organic-inorganic nanocomposite materials. *Chem. Mater.* **13**, 3169–3183 (2001).
31. Katsounaros, I., Cherevko, S., Zeradjanin, A. R. & Mayrhofer, K. J. J. Oxygen electrochemistry as a cornerstone for sustainable energy conversion. *Angew. Chem. Int. Ed.* **53**, 102–121 (2014).
32. Treimer, S., Tang, A. & Johnson, D. C. A consideration of the application of Koutecky-Levich plots in the diagnoses of charge-transfer mechanisms at rotated disk electrodes. *Electroanal.* **14**, 165–171 (2002).
33. Li, X., Qu, W., Zhang, J. & Wang, H. Electrocatalytic activities of La₀.₆C₀.₆CoO₃ and La₀.₆Ca₀.₄CoO₃-carbon composites toward the oxygen reduction reaction in concentrated alkaline electrolytes. *J. Electrochem. Soc.* **158**, A597–A604 (2011).

34. Sunarso, J., Torriero, A. A. J., Zhou, W., Howlett, P. C. & Forsyth, M. Oxygen reduction reaction activity of La-based perovskite oxides in alkaline medium: a thin-film rotating ring-disk electrode study. *J. Phys. Chem. C* **116**, 5827–5834 (2012).

35. Rios, E., Gautier, J.-L., Poillerat, G. & Chartier, P. Mixed valency spinel oxides of transition metals and electrocatalysis: case of the $Mn_xCo_{3-x}O_4$ system. *Electrochim. Acta* **44**, 1491–1497 (1998).

36. Cheng, F. *et al.* Rapid room temperature synthesis of nanocrystalline spinels as oxygen reduction and evolution electrocatalysts. *Nat. Chem.* **3**, 79–84 (2011).

37. Li, J., Xiong, S., Li, X. & Qian, Y. A facile route to synthesize multiporous $MnCo_2O_4$ and $CoMn_2O_4$ spinel quasi-hollow spheres with improved lithium storage properties. *Nanoscale* **5**, 2045–2054 (2013).

38. Fu, C. *et al.* One-step calcination-free synthesis of multicomponent spinel assembled microspheres for high-performance anodes of Li-ion batteries: a case study of $MnCo_2O_4$. *ACS Appl. Mater. Interfaces* **6**, 2439–2449 (2014).

39. Schmidt, T. J. *et al.* Characterization of high-surface-area electrocatalysts using a rotating disk electrode configuration. *J. Electrochem. Soc.* **145**, 2354–2358 (1998).

Acknowledgments

Author contributions

Additional information